Magnetic Energy Storage and Current Density Distributions for Different Force-Free Models

S. Régnier

Abstract
   In the last decades, force-free-field modelling has been used extensively to describe the coronal magnetic field and to better understand the physics of solar eruptions at different scales. Especially the evolution of active regions has been studied by successive equilibria in which each computed magnetic configuration is subject to an evolving photospheric distribution of magnetic field and/or electric current density. This technique of successive equilibria has been successful in describing the rate of change of the energetics for observed active regions. Nevertheless the change in the magnetic configuration due to the increase/decrease of electric current for different force-free models (potential, linear and nonlinear force-free fields) has never been studied in detail before. Here we focus especially on the evolution of the free magnetic energy, the location of the excess of energy, and the distribution of electric currents in the corona. For this purpose, we use an idealised active region characterised by four main polarities and a satellite polarity allowing us to specify a complex topology and sheared arcades to the coronal magnetic field but no twisted flux bundles. We investigate the changes in the geometry and connectivity of field lines, the magnetic energy and current density content as well as the evolution of null points. Increasing the photospheric current density in the magnetic configuration does not dramatically change the energy-storage processes within the active region even if the magnetic topology is slightly modified. We conclude that for reasonable values of the photospheric current density (the force-free parameter $\alpha < 0.25$ Mm^{-1}), the magnetic configurations studied do change but not dramatically: *i*) the original null point stays nearly at the same location, *ii*) the field-line geometry and connectivity are slightly modified, *iii*) even if the free magnetic energy is significantly increased, the energy storage happens at the same location. This extensive study of different force-free models for a simple magnetic configuration shows that some topological elements of an observed active region, such as null points, can be reproduced with confidence only by considering the potential-field approximation. This study is a preliminary work aiming at understanding the effects of electric currents generated by characteristic photospheric motions on the structure and evolution of the coronal magnetic field.

[1] Jeremiah Horrocks Institute, University of Central
Lancashire, Preston, Lancashire, PR1 2HE, UK
email: SRegnier@uclan.ac.uk

1. Introduction

One key unsolved issue in solar physics is the generation and effects of electric currents from photospheric motions of the stressed and sheared coronal magnetic field. With the development of reliable techniques such as coronal magnetic-field extrapolations based on complex distributions of photospheric currents (see *e.g.*, reviews by Régnier, 2007; Wiegelmann, 2008), it is important to understand how a modelled magnetic-field configuration is subject to change due to slight modifications of the photospheric-current distribution and thus the difference between several force-free assumptions using the same boundary conditions. The main aim is to understand these changes in the geometry and topology of field lines assuming that the magnetic field is in a force-free equilibrium. In Régnier and Priest (2007), we have performed a first comparison between four different active regions with different behaviours due to the complex distribution of the photospheric field and of the electric currents representing the history of the evolution of the active region. This comparison was done for the same force-free model, namely the nonlinear force-free field. We showed that, statistically speaking, the magnetic-field lines are longer and higher in a nonlinear force-free field compared to the corresponding potential field. To develop our understanding of the effects of electric currents on magnetic configurations, Régnier (2009) compared the behaviour of a simple bipolar field subject to different distributions of electric currents using different force-free models. The bipolar field has been studied in terms of magnetic-energy storage and magnetic-helicity changes. We showed that the amount of electric currents that can be injected in a magnetic-equilibrium configuration depends strongly on the spatial distribution of the currents, the existence of return currents having a stabilising effect on the magnetic configuration. The next step developed in this article is to understand the effects of electric currents on a magnetic configuration having predominant topological elements (*i.e.* a null point in the domain of interest).

In the past decades, magnetic topology has become a key ingredient in understanding the origin of flares in active regions.

The general definition of magnetic topology concerns the properties of magnetic-field lines and magnetic-flux surfaces that are invariant under continuous deformation in plasma conditions satisfying the frozen-in assumption (Low, 2006; Low, 2007; Janse, Low, and Parker, 2010; Berger and Prior, 2006). This definition implies that the number of null points does not change and the connectivity of field lines rigidly anchored to the boundaries of the domain is also invariant under the above conditions. However, we focus here on the evolution of topological elements and connectivity of field lines obtained from force-free models: the field lines are not rigidly anchored (the models allow for reconnection of field lines) in order to maintain a force-free state. Since the magnetic topology is not required to be preserved, we restrict the definition of the magnetic topology for a given equilibrium state to the ensemble of topological elements forming

the magnetic skeleton (Bungey, Titov, and Priest, 1996). Despite an extensive literature on magnetic topology, the theoretical background in three dimensions was developed only recently (see review by Priest and Forbes, 2000). The 3D topological elements constituting the skeleton of a magnetic configuration can be divided into two parts: the true topology containing null points, separatrix surfaces, and separators, and the quasi-topology including quasi-separatrix layers and hyperbolic flux tubes (and the true topology). We focus especially on the location and properties of null points as a proxy for describing the topology of magnetic configuration. This study aims at understanding the possible changes of properties and location of null points subject to the continuous variation of a free parameter in various force-free models.

It has been proven that the topological elements of a coronal magnetic configuration are of prime importance to study the onset of flares and coronal mass ejections (CMEs). For instance, in the classical model of flare, magnetic reconnection occurs at a null point or in a current sheet formed along a topological element. Combining observations and coronal-field models, Aulanier *et al.* have shown that a powerful flare associated with a CME involves a coronal null point and a spine field line. This topological study in conjunction with EUV observations supports the breakout model (Antiochos, Devore, and Klimchuk, 1999) as a triggering mechanism for this particular event. Recently, Zhao *et al.* (2008) have derived the skeleton of an active region and its temporal evolution before and after an eruptive event. The authors have found several coronal null points in a quasi-force-free field configuration. Unfortunately, the null points found by Zhao *et al.* (2008) did not satisfy the properties of null points for force-free fields and for divergence-free fields (see Appendix A). Other topological studies have been carried out to better understand the release of magnetic energy and the reconnection processes in active region evolution (Démoulin, Hénoux, and Mandrini, 1994; Deng *et al.*, 2005; Barnes, Longcope, and Leka, 2005; Régnier and Canfield, 2006; Li *et al.*, 2006; Luoni *et al.*, 2007; Barnes, 2007), during blinkers (Subramanian *et al.*, 2008), and in the quiet Sun (Schrijver and Title, 2002; Close, Heyvaerts, and Priest, 2004; Régnier, Parnell, and Haynes, 2008)

Our work has been motivated by two earlier articles on this topic by Démoulin, Hénoux, and Mandrini (1994) and Hudson and Wheatland (1999). Démoulin, Hénoux, and Mandrini (1994) have compared the topology of potential and linear force-free fields for a quadrupolar configuration with a coronal null. They found that the topology is similar for the point-charge model but they also noticed that for a bipolar model (based on extended sources) another null can be created in the linear force-free configuration for large value of the force-free parameter α. Based on the point-charge model, Bungey, Titov, and Priest (1996) reached the same conclusion for different charge distributions. Hudson and Wheatland (1999) have considered a quadrupolar point charge, symmetric distribution to study the connectivity of field lines for potential, linear, and nonlinear force-free fields. They concluded that the topology can be insanely different from one model to the other. For non-symmetric cases, Brown and Priest (2000) have found that the topology of a force-free configuration can be similar using the point-charge model. As a step forward to the understanding of the magnetic topology of reconstructed coronal fields, we carry out a comparison between

different models of magnetic fields (potential, linear, and nonlinear force-free fields) for a configuration having a coronal null point assuming a continuous distribution of magnetic field at the bottom boundary and no symmetry. We describe the changes in the magnetic configurations based on the evolution of the geometry and connectivity of magnetic field lines and in terms of distribution of magnetic energy and electric currents. In addition, we study the properties of null points as a proxy of the complexity of the field, keeping in mind that the separators and separatrices play an important role in the release of magnetic energy (*e.g.*, Priest, Longcope, and Heyvaerts, 2005). It is worth noticing that we only focus on the modelling of magnetic-field equilibria and their changes through the increase of electric currents, whilst recently Santos, Büchner, and Otto (2011) have described the changes in magnetic fields subject to characteristic photospheric motions using a magnetohydrodynamic (MHD) approach. They have found that the topology of a quadrupolar magnetic field remains stable whatever the perturbations imposed even in the case of strong currents. The authors claimed that their results can easily be generalised to more complex magnetic-field distributions and non-generic and symmetric cases. Despite their sophisticated MHD approach, they do not study the changes in magnetic energy or in the connectivity of field lines.

In Section 2.1, we construct a magnetic configuration with a coronal null point from which we will reconstruct the different models (see Section 2.2). We thus analyse the geometry of field lines in Section 3 and their connectivity in Section 4. The change in topology in the different models is discussed in Section 5. In addition, we study how the magnetic energy is stored (Section 6) and the electric currents are concentrated (Section 7). In Section 8, we discuss the implications for future topological studies from reconstructed magnetic fields.

2. Constructing a Coronal Null Point

2.1. The Potential-Field Distribution

We first build a quadrupolar distribution of the vertical component of the magnetic field (B_z) at the bottom boundary (see Figure 1 left). The polarities are defined as Gaussian distributions with the field strength at the centre and the width of the distribution as free parameters: N1 and N2 (P1 and P2) are negative (positive) polarities. To realistically model a solar active region, we assume that the spatial resolution is of 1 Mm giving a characteristic size of 140 Mm. The four polarities are placed such that there is no symmetry. Each polarity has a maximum field strength of 2000 G in absolute value and a different width of the Gaussian distribution. The total magnetic flux is balanced.

From the magnetogram depicted in Figure 1 left, we compute the potential field in the coronal volume (Ω: 140 pixels×140 pixels×120 pixels) imposing closed boundary conditions on the sides and top of the computational box. Few magnetic field lines have been selected in Figure 1 right to show the geometry and topology of the potential field associated with this quadrupolar distribution. There is no null point in the potential-field configuration. However, the magnetic
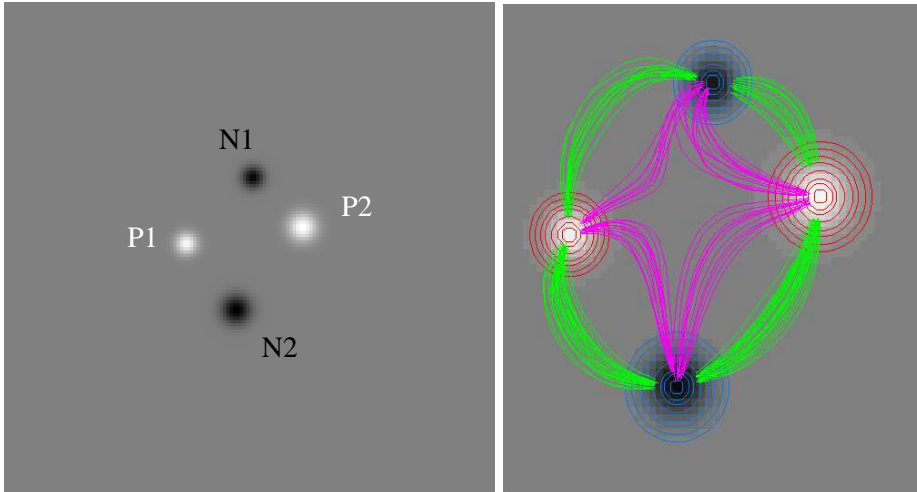
Figure 1. (Left) Quadrupolar distribution of the vertical component of the magnetic field (B_z) used as initial field (black and white are negative (N1 and N2) and positive (P1 and P2) polarities). The total magnetic flux is balanced. (Right) Close-up of a few field lines (red and green) depicting the geometry and topology of the potential-field configuration. White polarities and red contours (black polarities and blue contours) are positive (negative) values of B_z.

configuration has a topology characterised by quasi-separatrix layers (QSLs) as shown, in Figure 1 right, by the red field lines dividing the domain in four distinct regions. The study of the QSLs is beyond the scope of this article. We note that the simplest magnetic configuration with a topology is a configuration with three polarities as studied in detail by Brown and Priest (1999). We have chosen a quadrupolar configuration in order to confine the null point inside the strong-field region.

To create a coronal null point, we emerge a polarity N3 (negative in this experiment) at the location where there is a field-strength minimum of the quadrupolar distribution (see Figure 2 left). The total magnetic flux is kept balanced. We then compute the potential field associated with this new magnetogram, and with the same boundary conditions as in the quadrupolar case. The height of the null point depends on the field strength of the polarity N3: for a maximum field strength of –800 G, the null point is located 6.9 Mm above the bottom boundary (see also Table 1). In the following experiment, we will use the vertical component of the magnetic field depicted in Figure 2 left as a boundary condition for the different force-free models.

2.2. The Magnetic-Field Models

The Grad–Rubin Algorithm

The computed linear and nonlinear force-free fields are based on the Grad and Rubin (1958) numerical scheme described by Amari *et al.* (1997, 1999) and Amari, Boulmezaoud, and Aly (2006). The same boundary conditions are used
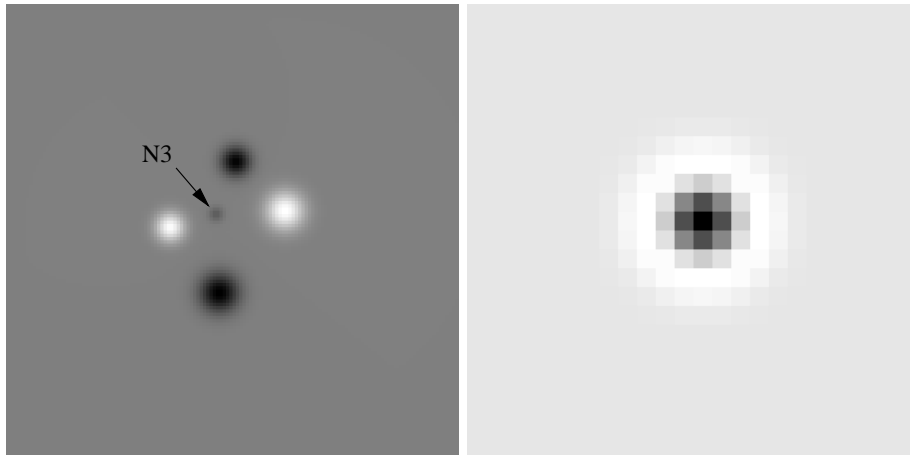
Figure 2. (Left) Distribution of the vertical component of the magnetic field at the bottom boundary (black and white for negative and positive polarities); (Right) Typical ring distribution of J_z that we impose on the positive polarities

for all the models: the vertical magnetic-field component everywhere and the distribution of α in one chosen polarity on the bottom boundary, and closed boundary conditions on the sides and top of the computational box. Using the same boundary conditions for all models allows us to perform a direct comparison of the magnetic energy and the topology of the different magnetic configurations.

The force-free field in the volume above the bottom boundary is thus governed by the following equations:

$$\nabla \times \mathbf{B} = \alpha \mathbf{B}, \tag{1}$$

$$\mathbf{B} \cdot \nabla \alpha = 0, \tag{2}$$

$$\nabla \cdot \mathbf{B} = 0, \tag{3}$$

where $\mathbf{B}$ is the magnetic-field vector in the domain Ω above the photosphere ($\delta\Omega$), and α is a function of space defined as the ratio of the vertical current density (J_z), and the vertical magnetic field component (B_z). From Equation (2), α is constant along a field line. In terms of the magnetic field $\mathbf{B}$, the Grad–Rubin iterative scheme can be written as follows:

$$\mathbf{B}^{(n)} \cdot \nabla \alpha^{(n)} = 0 \quad \text{in} \quad \Omega, \tag{4}$$

$$\alpha^{(n)}|_{\delta\Omega^\pm} = h, \tag{5}$$

where $\delta\Omega^\pm$ is defined as the domain on the photosphere for which B_z is positive (+) or negative (−) and,

$$\nabla \times \mathbf{B}^{(n+1)} = \alpha^{(n)} \mathbf{B}^{(n)} \quad \text{in} \quad \Omega, \tag{6}$$

$$\nabla \cdot \mathbf{B}^{(n+1)} = 0 \quad \text{in} \quad \Omega, \tag{7}$$

$$B_z^{(n+1)}|_{\delta\Omega} = g, \tag{8}$$

$$\lim_{|r|\to\infty} |\mathbf{B}| = 0. \tag{9}$$

The boundary conditions on the photosphere are given by the distribution (g) of B_z on $\delta\Omega$ (see Equation (8)) and by the distribution (h) of α on $\delta\Omega$ for a given polarity (see Equation (5)). We also impose that

$$B_n = 0 \quad \text{on} \quad \Sigma - \delta\Omega \tag{10}$$

where Σ is the surface of the computational box, n refers to the component normal to the surface. These conditions mean that no field line can enter or leave the computational box. To ensure the latter condition, we have chosen a bottom boundary large enough for the magnetic-field strength to tend to zero near the edges of the field-of-view.

Linear Force-Free Fields

The linear force-free models are based on the Grad–Rubin algorithm where the distribution of α is a constant. We choose values of α ranging from –1 to 1 Mm^{-1} with a step $\delta\alpha = 0.02$ Mm^{-1}. These α values correspond to active-region values reported, for instance, by Leka and Skumanich (1999) and computed by assuming that the measured photospheric field is force-free.

Nonlinear Force-Free Fields

In addition to the vertical component of the magnetic field, the Grad–Rubin scheme requires a distribution for the current density (or α) in order to derive the nonlinear force-free field. Our choice goes to the so-called *ring* distribution defined by a second-order Hermite polynomial function as follows:

$$J_z = 2\, J_{z0}\, [r^2 - C_0]\, \exp\left(-\frac{r^2}{\sigma^2}\right), \tag{11}$$

where r is measured from the centre of the source and C_0 is a constant that ensures a zero net current. An example of ring distribution is depicted in Figure 2 right. For the sake of comparison, we choose J_{z0} [-20, -10, 10, 20] mA m^{-2}, which are characteristic values of the current density in active regions as has been measured in the photosphere from vector magnetograms (*e.g.*, Leka and Skumanich, 1999). The distribution of α is then given by:

$$\alpha = \frac{\mu_0 J_z}{B_z}. \tag{12}$$

In accordance with the Grad–Rubin mathematically well-posed boundary-value problem, we impose the distribution of α in one chosen polarity (the positive
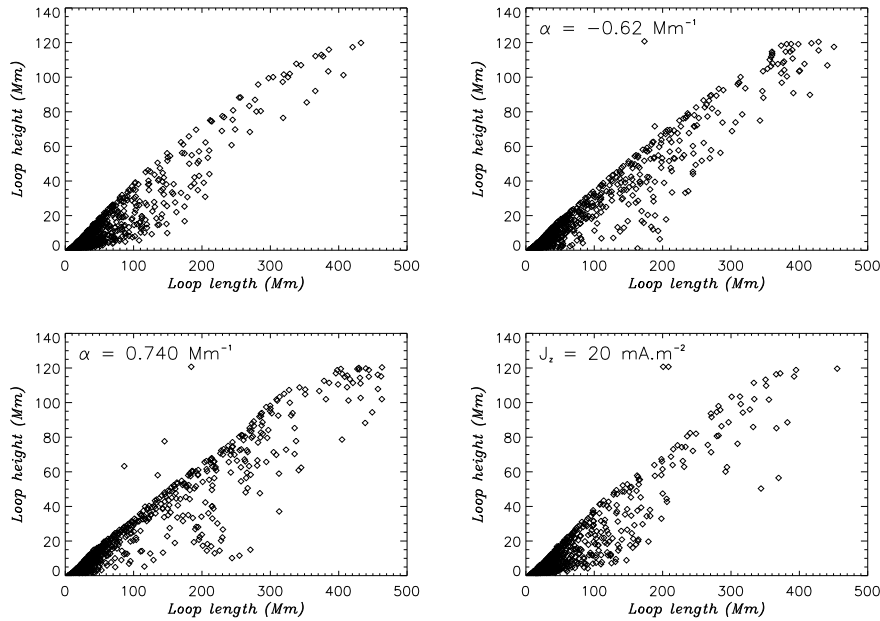
Figure 3. Scatter plots of the length and height of selected field lines for (a) the potential field, (b) and (c) the linear force-free field with $\alpha = -0.62, 0.74$ Mm^{-1} respectively, and (d) the nonlinear force-free field with $J_{z0} = 20$ mA m^{-2}.

polarities in this experiment) as boundary condition for the nonlinear force-free field. We use the same grid and the same side and top boundary conditions as for the potential and linear force-free fields.

This particular choice of the vertical current distribution is justified by the study reported by Régnier (2009), which analysed the behaviour of a simple bipolar field under the assumption of a nonlinear force-free field by using several distribution of J_z (or α). This study showed that the ring distribution of current gives magnetic configurations that are more stable and in which a large amount of current can be injected. The conclusion is easily explained by the stabilising effects of the return currents. Ring-current distributions have been used before for simulating twisted flux tubes in MHD models (Magara and Longcope, 2003).

3. Statistical Study of Field-Line Geometry

To study the differences between the different magnetic configurations obtained for each model, the first step is to analyse the changes in the geometry of field lines. So we first select field lines by considering their footpoints with a field strength above 100 G in absolute value. In the following, we will focus on four different distributions which are characteristic of this study: the potential field, two linear force-free field configurations for $\alpha = -0.62, 0.74$ Mm^{-1} and one nonlinear force-free field with $J_{z0} = 20$ mA m^{-2}.
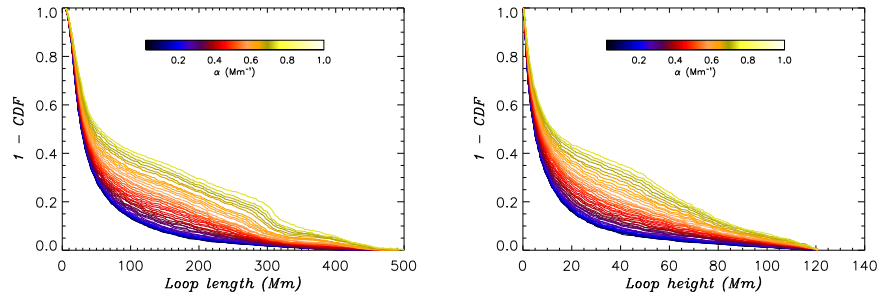
Figure 4. Cumulative distribution function (CDF) for the linear force-free models (coloured curves for the different values of α) for the field-line length (left) and the field line height (right). We only plot the distribution for positive values of α to avoid confusion.

In Figure 3, the scatter plots of the length and height of the selected field lines are shown for the four configurations. It is clear that the injection of electric currents in a magnetic configuration changes, in a statistical sense, the geometry of field lines compared to the potential field but not the same way for each model. The changes in geometry are more pronounced for the linear force-free models whilst the geometry remains similar for the nonlinear force-free field. As mentioned above, the similarity of the nonlinear force-free model and the potential field and the differences with the linear force-free fields are due to the existence of return currents and their stabilising effects. We now study more closely how the changes in the geometry of field lines evolve when the current density is increased. In Figure 4, we plot the cumulative-distribution functions of the length (left) and height (right) of selected field lines. We determine that 50% of the field lines are shorter than 25 Mm and lower than 5 Mm for the potential field whilst 50% of the field lines reaches 50 Mm in length and 15 Mm in height for $\alpha = 1$ Mm^{-1}. The differences between the different linear force-free models occur for field lines longer than 50 Mm and higher than 10 Mm. We also notice that the main differences occur for values of α greater than 0.25 Mm^{-1}. The CDFs are consistent with the analysis of Régnier and Priest (2007): by studying the force-free-field configurations of four different active regions, the authors have concluded that, statistically, the field lines in a nonlinear force-free field are longer and higher than for the corresponding potential field configuration. We will later refer to values of α less than 0.25 Mm^{-1} as reasonable values of α.

4. Field-Line Connectivity

To depict the connectivity of the field lines, we associate, on a 2D map, the location of the footpoint of a field line to their length. The connectivity plots are drawn for the four characteristic force-free fields in Figure 5. We first notice that the connectivity of the parasitic polarity is not modified for the different models. The changes of connectivity mostly affect the field lines on the outer edges of the polarities and not the regions of strong magnetic-field concentrations. It is worth noticing that the Grad–Rubin algorithm computes the nonlinear force-free field
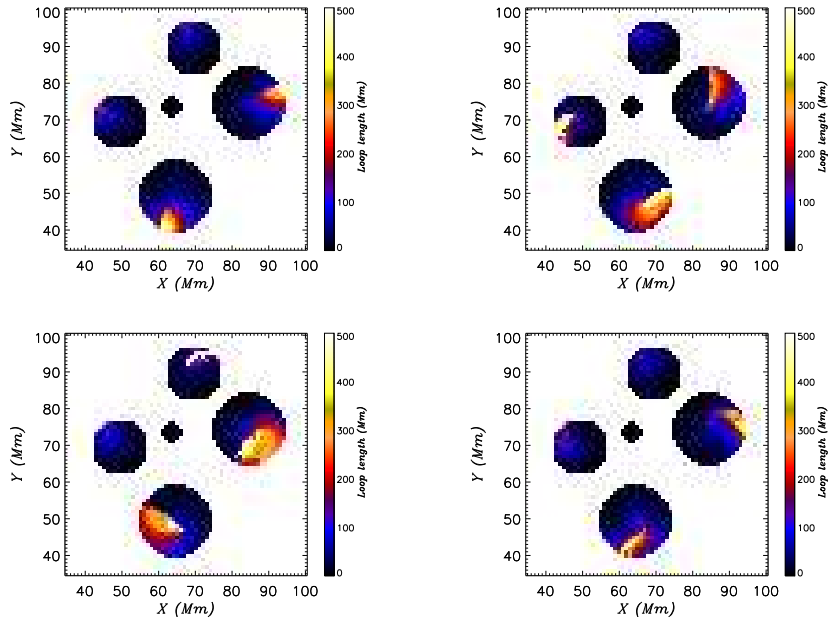
Figure 5. Connectivity maps for a restricted field of view (x=[30, 110], y=[30, 110]) depicting the field lines having the same length for the potential field (top left), the force-free field with $\alpha = -0.62$ Mm^{-1} (top right) and $\alpha = 0.74$ Mm^{-1} (bottom left), and the nonlinear force-free field with $J_{z0} = 20$ mA m^{-2} (bottom right). The colour bar indicates the loop lengths in Mm.

from the positive polarities. For the linear force-free fields, we notice that the long field lines are moved counter-clockwise (clockwise) when the negative (positive) values of α are increased in absolute value. For the nonlinear force-free field, a positive (negative) value of J_{z0} gives the same behaviour as a negative (positive) value of α in the linear force-free configurations. Therefore the connectivity of field lines depends strongly on the amount of electric currents injected in the magnetic configurations.

5. Null Point Properties

5.1. Location of Null Points

We locate the null points within the magnetic configurations using the trilinear interpolation method developed by Haynes and Parnell (2007). We then compare the location of the null points for the different models. We plot the location of the null points onto the x–y-plane for the potential field in Figure 6, for the linear force-free fields with α between –1 and 1 Mm^{-1} in Figure 7 left, and for the nonlinear force-free fields using several values of J_{z0} in Figure 7 right. There is only one null point NP0 in the potential field located 6.9 Mm above the parasitic negative polarity (see Figure 6). In Figure 7, the null points present in
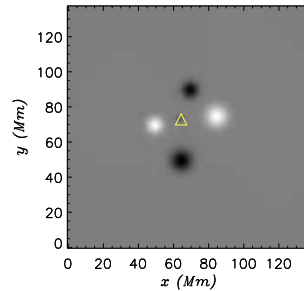
Figure 6. Location of the null point (yellow triangle) located at $z = 6.9$ Mm in the potential field configuration. The background image is the distribution of the vertical component of the magnetic field (black and white for negative and positive polarities).

the magnetic configuration for both the linear and nonlinear force-free fields can be divided into two groups:

i) near the location of the potential null point, a null point is found for all models whatever the value of the current density or the force-free parameter α;

ii) other null points can appear mostly near the boundaries but also in strong field regions.

For the first group, we conclude that the null point NP0 created in the potential field is stable in the other models and its location is just slightly influenced by the current density: the null point is moving up and down, left and right depending on the sign of the current density. For the second group, we can already notice that most of the null points are located near the side boundaries, and in addition the null point NP1 is moving towards strong field regions when α is increased (see Figure 7 left). However, we need to investigate the properties of the null point to draw conclusions (see Section 5.2).

In Figure 8, we plot the distribution of null points as a function of height for the linear force-free configurations. We indicate the sign of the null points: triangles (resp. diamonds) for positive (resp. negative) null points. This plot allows us to track the null points depending on the value of the parameter α and on the sign of the null points. We notice that the potential-field null point NP0 evolves smoothly when the α parameter (in absolute value) increases: the null point height varies continuously from 4 Mm to 7.5 Mm whilst the null point height in the potential field is 6.9 Mm as indicated by the dashed line in Figure 8 (see also Table 1).

Other null points appear when $|\alpha| > 0.1$ Mm^{-1} (see Figure 8). We obtain up to five null points at $\alpha \approx 0.7$ Mm^{-1} (see Table 1). Several null points are located near the bottom boundary. All null points are at a height less than 40 Mm (one-third of the vertical length of the computational box) where the bipolar field is dominant: the complexity of the quadrupolar and parasitic polarities is located below 40 Mm. Note that the bipolarisation of the magnetic field and its associated height are also measures of the complexity of the magnetic field.
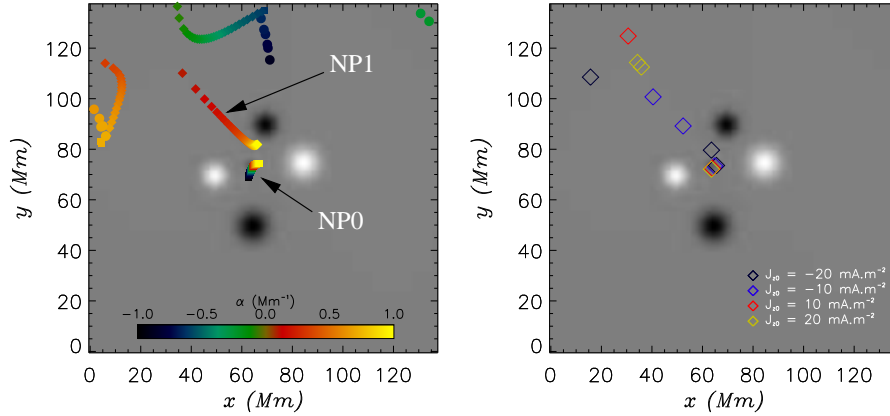
Figure 7. Same as Figure 6: (Left) linear force-free fields with α varying from -1 to 1 Mm^{-1}. NP0 is depicted by a square symbol whilst other null points are depicted by a diamond (circle) symbol when their height is greater (lower) than NP0. (Right) nonlinear force-free fields with $J_{z0} = [-20, -10, 10, 20]$ mA m^{-2} (diamonds).
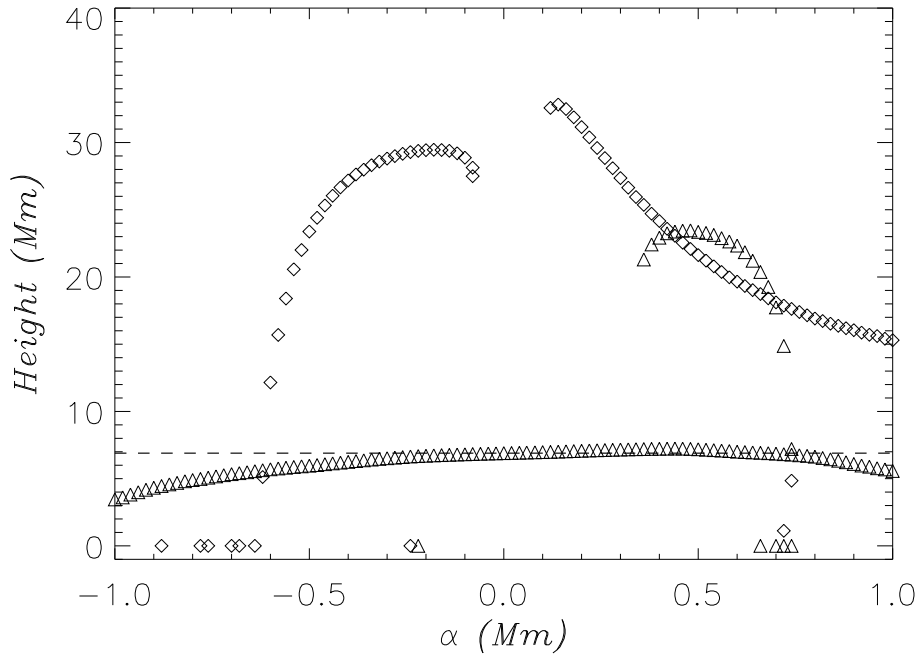

Figure 8. Height of the null points in the potential and linear force-free field models for α varying from –1 to 1 Mm^{-1}. The dashed line indicates the height of NP0 in the potential configuration. Triangles (diamonds) indicate positive (negative) null points.

The height of the stable null point decreases when α is negative and it increases when α is positive. Nevertheless for $\alpha > 0.5$ Mm^{-1}, the height starts to decrease, influenced by the null point NP1 propagating in the strong field region towards NP0 (see Figure 7 left).

In Figure 7 right, we find the same groups of null points for the nonlinear force-free fields. We note that, for this experiment, a nonlinear force-free field with negative (positive) values of J_{z0} has the same behaviour as a linear force-free field with positive (negative) values of α.

5.2. Properties

As discussed in Appendix A, the null points can be classified as negative and positive depending on whether the fan field lines are radiating in or out, respectively, from the null point. To derive the spectral properties of a null point, we first need to derive the Jacobian matrix and then to compute the eigenvalues. To describe these properties, we thus introduce a quantity which helps us to classify the nature of the null points: the spectral radius of the Jacobian matrix (ρ_J) as follows:

$$\rho_J = \max_i \left(|\lambda_i| \right) \quad \text{for} \quad i = 1, 2, 3 \tag{13}$$

where λ_i are the (real or complex) eigenvalues of the Jacobian matrix. For a Jacobian matrix having two complex-conjugate eigenvalues, the spectral radius (ρ_J) is the real eigenvalue for a divergence-free magnetic field.

In Table 1, we summarize the properties of the null points (type, location, eigenvalues, spectral radius) for the potential field, the linear force-free fields with $\alpha = [-0.62, 0.74]$ Mm^{-1}, and the nonlinear force-free fields with $J_{z0} = [-20, -10, 10, 20]$ mA m^{-2}. The eigenvalues are sorted in such way that the spectral radius corresponds to the absolute value of the first eigenvalue. The null point present in the potential configuration is a positive null point with one negative and two positive eigenvalues. This null point (NP0) is also present in the linear and nonlinear force-free configurations with a slight displacement up and down, left and right depending on the sign of the α values. Thus, the null point (NP0) originally created in the potential field is stable for all force-free models. In particular, NP0 is always a positive null point and the spectral radius is almost constant. Therefore we conjecture that the spectral radius gives a good proxy for the stability of a null point in a magnetic-field configuration. Note that a large spectral radius indicates large magnetic-field gradients.

In addition to NP0, other null points can appear in the magnetic configuration depending on the strength of the current density. It is noticeable that null points are mostly created in pairs (negative and positive null points) or they have complex eigenvalues. The latter case which indeed cannot exist in the force-free assumption corresponds to null points appearing at locations where *i*) the Taylor expansion in the vicinity of the null point is not valid anymore, or *ii*) the null-point finder algorithm breaks down, or *iii*) the Jacobian matrix elements cannot be derived with enough accuracy (especially in weak-field regions). Note that we only found four values of α (among 120) for which complex conjugate eigenvalues exist.

Table 1. Properties of null points (type, location, eigenvalues) for the potential, linear force-free fields with $\alpha = [-0.62, 0.74]$ Mm^{-1} and nonlinear force-free fields with $J_{z0} = [-20, -10, 10, 20]$ mA m^{-2}. [a] One real and two complex eigenvalues (only the real parts are reported).

Model	α or J_{z0}	Type	Location (x_0, y_0, z_0)	Eigenvalues $(\lambda_1 = \pm\rho_J, \lambda_2, \lambda_3)$
Potential		$+$	(64.30, 72.94, 6.90)	$(-\mathbf{0.026}, 0.021, 5.5\ 10^{-3})$
Linear	-0.62	$+$	(63.43, 71.2, 5.63)	$(-\mathbf{0.032}, 0.023, 9.28\ 10^{-3})$
Force-Free		$-$	(68.8, 134.9, 5.12)	$(9.26, -4.8, -4.8) \times 10^{-5}$ [a]
(α)	0.74	$+$	(65.8, 74.2, 6.78)	$(-\mathbf{0.026}, 0.021, 5.7\ 10^{-3})$
		$+$	$(6.14, 85.2, 6\ 10^{-4})$	$(-2.68, 2.28, 0.836) \times 10^{-4}$
		$-$	(64.31, 81.63, 17.62)	$(5.8, -4.5, -1.0) \times 10^{-3}$
		$-$	(4.22, 83.12, 4.85)	$(5.83, -3.17, -3.17) \times 10^{-5}$ [a]
		$+$	(4.58, 82.44, 7.21)	$(-10, 4.86, 4.86) \times 10^{-5}$ [a]
Nonlinear	-20	$+$	(65.54, 73.57, 6.31)	$(-\mathbf{0.024}, 0.019, 4.86\ 10^{-3})$
Force-Free		$-$	(63.54, 79.64, 17.23)	$(4.71, -3.78, -0.88) \times 10^{-3}$
(J_{z0})		$+$	(15.70, 108.5, 36.98)	$(-4.38, 3.72, 0.35) \times 10^{-5}$
	-10	$+$	(64.84, 73.39, 6.77)	$(-\mathbf{0.021}, 0.017, 4.55\ 10^{-3})$
		$-$	(52.33, 89.19, 30.59)	$(4.02, -3.83, -0.21) \times 10^{-4}$
		$+$	(40.44, 100.7, 36.39)	$(-1.17, 1.13, 0.028) \times 10^{-4}$
	10	$+$	(63.87, 72.49, 7.12)	$(-\mathbf{0.020}, 0.016, 4.24\ 10^{-3})$
		$-$	(30.59, 124.7, 0.06)	$(7.27, -6.62, -0.69) \times 10^{-5}$
	20	$+$	(63.53, 72.10, 7.65)	$(-\mathbf{0.024}, 0.019, 4.9\ 10^{-3})$
		$-$	(34.29, 114.3, 0.025)	$(7.6, -5.9, -1.9) \times 10^{-4}$
		$-$	(35.82, 112.5, 14.29)	$(6.8, -6.3, -0.66) \times 10^{-4}$

6. Magnetic Energy Budget

6.1. Total Magnetic Energy

In Figure 9, we plot the magnetic energy (E_m) above the potential-field energy (E_{pot}) in the computational volume (Ω). As the potential field is a minimum-energy state, E_m is always above E_{pot}. The latter inequality is true if and only if both the force-free and potential fields are computed with the same normal component of the magnetic field on each side of the computational box.

The energy curve as a function of α is similar to the second-order polynomial curve obtained in Figure 11 of Régnier and Priest (2007) for a solar active region. For α ranging from -1 to 1 Mm^{-1}, the magnetic energy of linear force-free fields is not more 50% of the potential-field energy. The curve of the free magnetic energy as a function of α is not symmetric with respect to the potential field
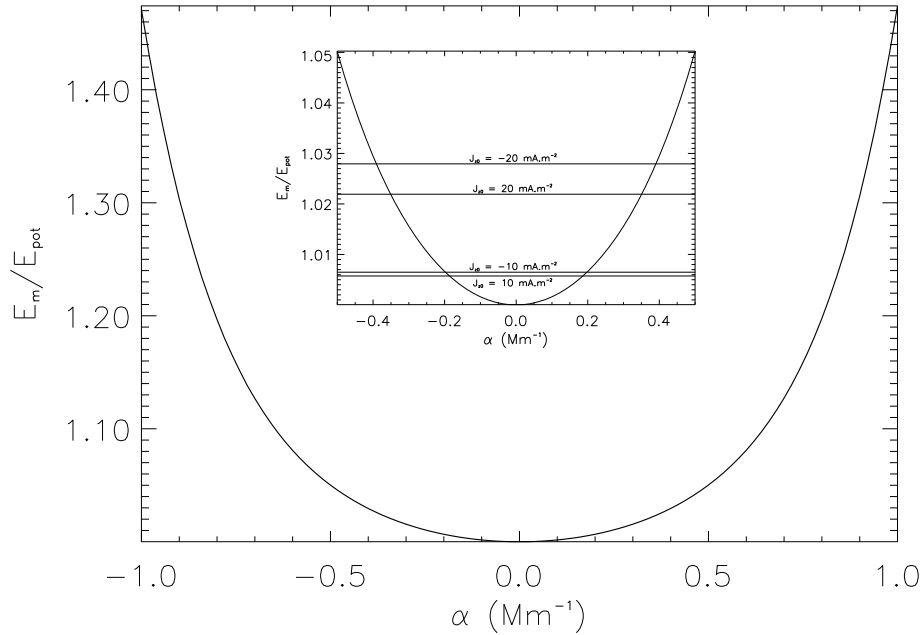
Figure 9. Magnetic energy (E_m) relative to the potential field energy ($E_{\rm pot}$) as a function of the force-free parameter (α: Mm^{-1}) for the linear force-free extrapolations. The solid lines indicate the relative energy levels $E_m/E_{\rm pot}$ for the nonlinear force-free extrapolations for $J_{z0} = [-20, -10, 10, 20]$ mA m^{-2}.

($\alpha = 0$): the magnetic energy is increasing more rapidly for the positive values of α.

The different levels of magnetic energy for the nonlinear force-free fields are plotted in Figure 9 as straight solid lines: $E_m/E_{\rm pot} = [1.0279, 1.0065, 1.0058, 1.022]$ for $J_{z0} = [-20, -10, 10, 20]$ mA m^{-2} respectively. This small amount of magnetic energy stored in the nonlinear force-free configurations (less than 3%) is a consequence of the particular current distribution: the ring distribution has no net current in a single polarity and return currents on the edges of the flux bundles which confine the magnetic field in strong-field regions without generating twisted flux bundles.

6.2. Energy Density Distributions

In Figure 10, we plot the magnetic-energy density integrated along the z-axis to study the distribution of the magnetic energy of the four magnetic fields analysed above. For the potential field, the distribution of the energy density is dominated by the energy (or field strength) near the bottom boundary for the five magnetic polarities. We notice that there is a local minimum of magnetic-energy density where the null point NP0 is located. In addition, there is another obvious local minimum located on the other side of the parasitic polarity with respect to NP0 (location: $x = 62, y = 78$). For the two linear force-free fields, the
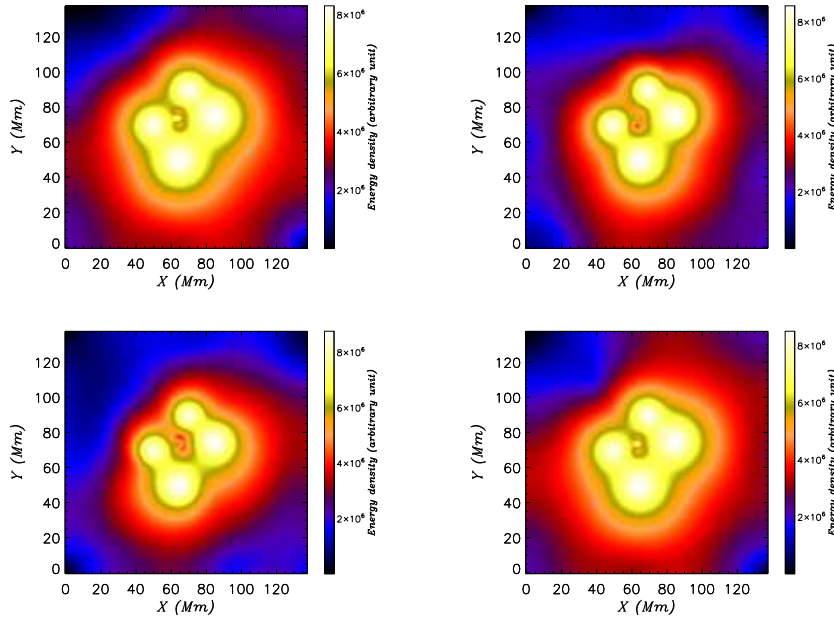
Figure 10. Energy-density maps integrated along the z-axis (in arbitrary unit) for the potential field (top left), the force-free field with $\alpha = -0.62$ Mm^{-1} (top right) and $\alpha = 0.74$ Mm^{-1} (bottom left), and the nonlinear force-free field with $J_{z0} = 20$ mA m^{-2} (bottom right). The colour bar indicates the energy density in arbitrary units.

magnetic-energy density distribution is dominated by the four polarities of the initial quadrupolar field where the magnetic-field strength is large, whilst the parasitic polarity does not influence the distribution. Again we notice that there is a strong local minimum at the location of NP0 and in addition there is an annulus-like series of local minima connecting NP0 and NP1 around the parasitic polarity. The other null points located in weak-field regions are not observed on the energy-density maps. For the nonlinear force-free field, the energy density distribution looks very much like the distribution of the potential field with a maximum of energy density slightly increased.

We notice that we are able to easily identify null points as local minima in the distribution of energy density where strong magnetic-field gradients are observed (large spectral radius).

7. Electric Currents

In Figure 11, we plot the electric-current density integrated along the z-axis for three of the four characteristic magnetic field computations. We have computed the three components of the current density from the curl of the magnetic field and then plotted the current-density strength (or modulus). The potential field has zero electric current (or only tiny currents due to the errors when the magnetic-field components are differentiated). The distribution of the current
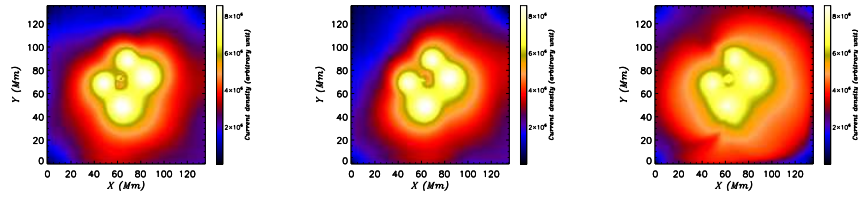
Figure 11. Electric-current density maps integrated along the z-axis for the force-free field with $\alpha = -0.62$ Mm^{-1} (left) and $\alpha = 0.74$ Mm^{-1} (middle), and the nonlinear force-free field with $J_{z0} = 20$ mA m^{-2} (right). The colour bar indicates the current density in arbitrary unit.

density is different from the distributions of the energy density (see Figure 10). The five polarities contribute a large amount to the current-density distribution. As noticed for the energy-density distribution, there exists a local minimum where the null point NP0 is located, and an annulus-like series of local minima exists connecting the null points NP0 and NP1 in the linear force-free fields. For the nonlinear force-free field configuration, the electric-current density distribution is similar to the linear force-free distribution with a local minimum at the location of NP0.

Except for the location of null points, it is not obvious wwhere to locate with this method the other topological elements where the current density is supposed to be increased. This shows that, for this configuration, the storage of current density along topological elements is not an efficient mechanism compared to the current density stored in the strong-field regions above the magnetic polarities.

8. Discussion and Conclusions

We investigated the changes in the magnetic-field configurations obtained for different force-free models (potential, linear, and nonlinear force-free fields) using the same boundary conditions. We analysed the changes in terms of geometry and connectivity of field lines, magnetic energy, and electric-current distributions. We performed this analysis for a continuous magnetic-field distribution with no symmetry. We imposed an electric-current distribution that we have proven to be stable when a large amount of current is injected into the magnetic configuration (Régnier, 2009). Despite the previous works on this topic, we have here provided an extended analysis of magnetic configurations with a topology that has never been performed before.

For this experiment, the initial configuration corresponds to a potential field with five sources (two large bipoles and one parasitic polarity) having a null point NP0 in the corona. By injecting currents in the magnetic configuration, the geometry and topology of the linear and nonlinear force-free configurations are modified such that:

- the geometry of the field lines is modified similarly to previous results obtained on the same topic: statistically, the field lines are higher and longer when the absolute value of electric current is increased;

- the connectivity of the field lines can be strongly modified near the topological elements (where the connectivity is changed rapidly);
- the initial null point NP0 is moved slightly up or down when the force-free parameter (α) varies but remains with the same basic properties, in particular the spectral radius remains almost constant;
- other null points (up to five) can appear in the magnetic configurations; most of them are located near the boundaries but one (NP1) which propagates towards the strong-field region when the current density is increased;
- the magnetic energy and current distributions can highlight the location of stable null points where strong magnetic-field gradients are present.

We also noticed that for reasonable values of the electric current injected or the force-free parameter α ($< 0.25 \ \mathrm{Mm}^{-1}$ in this experiment) the magnetic configuration is almost not modified compared to the potential-field configuration.

We thus state that null points existing in potential-field configurations are also present in force-free configurations with the same properties (*e.g.*, sign, spectral radius). This statement means that the null points found in a potential field with a large spectral radius can be considered as stable null points in other magnetic-field models. Even if true for this experiment we need to confirm this statement in a future statistical study of solar active region magnetic fields. It is important to note here that this statement is true *i*) when the force-free fields are computed with the same boundary conditions, *ii*) when there is no noise in the datasets. In Appendix B, we noe that the null points in potential-field configurations are slightly affected by boundary conditions (periodic, closed, ...), spatial resolution or size of field-of-view: the null point with the strongest spectral radius remains stable.

From this study, we also provide a benchmark for analysing the topology of a magnetic configuration: it is possible to retrieve important information about the topology just by analysing the distribution of magnetic energy density and of the electric current density in the volume. Moreover, we emphasize the importance of checking the divergence-free property of the magnetic field in the vicinity of a null point.

References

Amari, T., Boulmezaoud, T. Z., Aly, J. J.: 2006, *Astron. Astrophys.* **446**, 691–705. doi:10.1051/0004-6361:20054076.

Amari, T., Aly, J. J., Luciani, J. F., Boulmezaoud, T. Z., Mikic, Z.: 1997, *Solar Phys.* **174**, 129–149.

Amari, T., Boulmezaoud, T. Z., & Mikic, Z.: 1999, *Astron. Astrophys.*, **350**, 1051

Antiochos, S. K., Devore, C. R., Klimchuk, J. A.: 1999, *Astrophys. J.* **510**, 485–493.

Aulanier, G., DeLuca, E. E., Antiochos, S. K., McMullen, R. A., Golub, L.: 2000, *Astrophys. J.* **540**, 1126–1142. doi:10.1086/309376.

Barnes, G.: 2007, *Astrophys. J.* **670**, 53 – 56. doi:10.1086/524107.

Barnes, G., Longcope, D. W., Leka, K. D.: 2005, *Astrophys. J.* **629**, 561 – 571. doi:10.1086/431175.

Berger, M. A., Prior, C.: 2006, *J. Phys. A Math. General* **39**, 8321 – 8348. doi:10.1088/0305-4470/39/26/005.

Brown, D. S., Priest, E. R.: 1999, *Roy. Soc. London Proc. Ser. A* **455**, 3931 – 3951.

Brown, D. S., Priest, E. R.: 2000, *Solar Phys.* **194**, 197 – 204.

Bungey, T. N., Titov, V. S., Priest, E. R.: 1996, *Astron. Astrophys.* **308**, 233 – 247.

Close, R. M., Heyvaerts, J. F., Priest, E. R.: 2004, *Solar Phys.* **225**, 267 – 292. doi:10.1007/s11207-004-4279-5.

Démoulin, P., Hénoux, J. C., Mandrini, C. H.: 1994, *Astron. Astrophys.* **285**, 1023 – 1037.

Deng, N., Liu, C., Yang, G., Wang, H., Denker, C.: 2005, *Astrophys. J.* **623**, 1195 – 120. doi:10.1086/428821.

Grad, H., Rubin, H.: 1958, in *Proc. 2nd Int. Conf. on Peaceful Uses of Atomic Energy* , UN, Geneva **31**, 190.

Haynes, A. L., Parnell, C. E.: 2007, *Phys. Plasmas* **14**, 2107. doi:10.1063/1.2756751.

Hornig, G., Schindler, K.: 1996, *Phys. Plasmas* **3**, 781 – 791.

Hudson, T. S., Wheatland, M.S.: 1999, *Solar Phys. 186*, 301 – 310.

Janse, Å. M., Low, B. C., Parker, E.N.: 2010, *Phys. Plasmas* **17**(9), 092901. doi:10.1063/1.3474943.

Leka, K. D., Skumanich, A.: 1999, *Solar Phys.* **188**, 3 – 19.

Li, H., Schmieder, B., Aulanier, G., Berlicki, A.: 2006, *Solar Phys.* **237**, 85 – 100. doi:10.1007/s11207-006-0173-7.

Low, B. C.: 2006, *Astrophys. J.* **649**, 1064 – 1077. doi:10.1086/506586.

Low, B. C.: 2007, *Phys. Plasmas* **14**(12), 122904. doi:10.1063/1.2822151.

Luoni, M. L., Mandrini, C. H., Cristiani, G. D., Démoulin, P.: 2007, *Adv. Space Res.* **39**, 1382 – 1388. doi:10.1016/j.asr.2007.02.005.

Magara, T., Longcope, D. W.: 2003, *Astrophys. J.* **586**, 630 – 649.

Parnell, C. E., Smith, J. M., Neukirch, T., Priest, E. R.: 1996, *Phys. Plasmas* **3**, 759 – 770.

Priest, E. R., Forbes, T.: 2000, *Magnetic reconnection : MHD theory and applications*, Cambridge University Press, Cambridge, 34 – 37.

Priest, E. R., Longcope, D. W., Heyvaerts, J.: 2005, *Astrophys. J.* **624**, 1057 – 1071. doi:10.1086/429312.

Régnier, S.: 2007, *Mem. Soc. Astron. Ital.* **78**, 126.

Régnier, S.: 2009, *Astron. Astrophys.* **497**, 17 – 20. doi:10.1051/0004-6361/200811502.

Régnier, S., Canfield, R. C.: 2006, *Astron. Astrophys.* **451**, 319 – 330.

Régnier, S., Priest, E. R.: 2007, *Astron. Astrophys.* **468**, 701 – 709.

Régnier, S., Parnell, C. E., Haynes, A.L.: 2008, *Astron. Astrophys.* **484**, 47 – 50. doi:10.1051/0004-6361:200809826.

Santos, J.C., Büchner, J., Otto, A.: 2011, *Astron. Astrophys.* **525**, 3. doi:10.1051/0004-6361/201014758.

Schrijver, C. J., Title, A. M.: 2002, *Solar Phys.* **207**, 223 – 240.

Subramanian, S., Madjarska, M. S., Maclean, R. C., Doyle, J. G., Bewsher, D.: 2008, *Astron. Astrophys.* **488**, 323 – 329. doi:10.1051/0004-6361:20079315.

Wiegelmann, T.: 2008, *J. Geophys. Res. (Space Phys.)* **113**(A12), 3. doi:10.1029/2007JA012432.

Zhao, H., Wang, J. X., Zhang, J., Xiao, C. J., Wang, H.M.: 2008, *Chinese J. Astron. Astrophys.* **8**, 133 – 145. doi:10.1088/1009-9271/8/2/01.

Appendix

A. Null Point Description

As a first approximation, we assume that the magnetic field around the null point approaches zero linearly. The magnetic field ($\mathbf{B}$) near a neutral point can then be expressed as a first order Taylor expansion:

$$\mathbf{B} = M \cdot \mathbf{r}, \tag{14}$$

where M is the Jacobian matrix with elements $M_{ij} = \partial B_i / \partial x_j$ for all $i, j = 1, 2, 3$ and $\mathbf{r}$ is the position vector (x, y, z). The Jacobian matrix has some interesting properties:

  i) as the magnetic field is divergence-free, $\mathrm{Tr}(M) = 0$. This property holds at each point of the magnetic field configuration.
  ii) for potential and force-free fields which satisfy $\nabla \wedge \mathbf{B} = \mathbf{0}$ or $\nabla \wedge \mathbf{B} = \alpha \mathbf{B}$, M is symmetric at the location of the null point. Therefore, M has three real eigenvalues and the eigenvectors are orthogonal.

From the first property and for force-free fields, we obtain the following relationship between the three real eigenvalues $(\lambda_1, \lambda_2, \lambda_3)$:

$$\lambda_1 + \lambda_2 + \lambda_3 = 0, \tag{15}$$

meaning that two eigenvalues, λ_2 and λ_3 say, have the same sign, and that $|\lambda_1| = |\lambda_2 + \lambda_3|$ implying that $|\lambda_1| > |\lambda_2|, |\lambda_3|$. According to Parnell *et al.* (1996), the single eigenvalue (λ_1) defines the direction of the spine field line whilst the two other eigenvalues (λ_2, λ_3) indicate the directions of the fan plane. Therefore we can classify null points as positive null points with two positive and one negative eigenvalues, and negative null points with two negative and one positive eigenvalues. For a positive (negative) null point, the magnetic field lines in the fan plane are directed away from (towards) the null point, whereas the spine field line is pointing towards (away from) the null point. Following Hornig and Schindler (1996), a null point is unstable if $\det(M) = 0$. The determinant of M is

$$\det(M) = \prod_{i=1}^{3} \lambda_i, \tag{16}$$

with $\det(M) < 0$ for a positive null point and $\det(M) > 0$ for a negative one. For potential and force-free fields, null points are stable, except if one eigenvalue $(\lambda_2$ or $\lambda_3)$ vanishes reducing the null point to a 2D null point unstable in the 3D configuration. If λ_1 vanishes, then all eigenvalues have to be zero, and thus the first-order Taylor expansion is no longer valid and the null-point properties are thus derived from the Hessian matrix instead of the Jacobian matrix.

B. On the Topology of Potential Fields

In this article, we have studied in detail the topology of force-free fields for a distribution of photospheric magnetic field inducing the existence of a null point. In order to compare the magnetic energy and properties of the different configurations, we have used the same boundary conditions. But is a magnetic configuration modified when the boundary condition are changed? and is the topology influenced by the spatial scales of the bounded box? To address these question, we perform a comparison of different potential fields and different spatial scales.

B.1. Effect of Boundary Conditions

The above computation were performed using a Grad–Rubin numerical scheme and assuming closed boundary conditions on the sides and top of the computational box. We now compute the magnetic configurations for a potential field with open boundary conditions and with periodic boundary conditions. In Figure 12 top row, we plot the location of the null points for these new boundary conditions. This has to be compared to Figure 6. The location of NP0 is similar for all models and the spectral radius of NP0 is again the strongest (see Table 2). The potential field with periodic boundary conditions has created two negative null points near the sides of the computational box. The topology of the potential field is slightly influenced by the boundary conditions for this experiment.

B.2. Effect of Spatial Resolution

To study the effects of the spatial resolution on the topology of potential fields, we modify the pixel size by a factor of 0.5 and 2 (Figure 12 middle row). We also make sure that the total unsigned magnetic flux remains unchanged (variation less than 1%). The computations are carried out with periodic boundary conditions. NP0 is located nearly at the same location for both spatial resolutions. The other null points are similar to those appearing in the potential field with periodic conditions. The cluster of eight null points suggests that there is a null line at this location. The topology of the potential field is thus similar to the topology of the potential field with closed boundary conditions. We again emphasize that the spectral radius of NP0 remains almost constant and is the strongest (see Table 2).

B.3. Effect of Field-of-View

We now modify the field-of-view of the experiment but keeping the same spatial resolution and the same total unsigned magnetic flux. In Figure 12 bottom row, we plot the location of the null points for two different fields-of-view using a potential field with periodic conditions: we decrease or increase the number of pixels by 40 pixels in each direction (20 pixels on each edge). The properties of the null points are summarised in Table 2. The number of null points is the same for the different fields-of-view. The spectral radius of NP0 is similar and still the strongest. The topology of the magnetic configuration is almost not influenced by the field-of-view for this experiment. It is worth noticing that the field-of-view was modified in such way that there is no magnetic flux on the edges of the computational box as this would strongly influence the magnetic configuration and also that it would have unexpected effects due to the violation of the solenoidal condition.

Table 2. Properties of null points (type, location, eigenvalues) for the different potential fields

| Model	Type	Location (x_0, y_0, z_0)	Eigenvalues $(\lambda_1 = \pm\rho_J, \lambda_2, \lambda_3)$
Boundary Conditions			
Closed Boundaries	$+$	(64.30, 72.94, 6.90)	$(-\mathbf{0.026}, 0.021, 5.5\ 10^{-3})$
Open Boundaries	$+$	(63.3, 71.96, 7.39)	$(-\mathbf{0.019}, 0.016, 5.2\ 10^{-3})$
Periodic Boundaries	$+$	(62.93, 71.25, 7.91)	$(-\mathbf{0.023}, 0.017, 5.5\ 10^{-3})$
	$-$	(61.4, 123.8, 0.02)	$(8.6, -5.1, -3.5)\times 10^{-3}$
	$-$	(126, 12.15, 5.38)	$(2.3, 0.02, 2.28)\times 10^{-4}$
Spatial Resolution			
70×70×60	$+$	(31.7, 35.8, 3.91)	$(-\mathbf{0.047}, 0.035, 0.01)$
	$-$	(31.06, 61.75, 0.01)	$(1.9, -1.1, -0.7)\times 10^{-3}$
	$-$	(63.05, 6.51, 3.14)	$(4.73, -4.68, -0.04)\times 10^{-4}$
280×280×240	$+$	(127.37, 144, 15.84)	$(-\mathbf{0.011}, 2.8\ 10^{-3}, 8.7\ 10^{-3})$
	$-$	(124.74, 246.8, 0.022)	$(4.7, -2.76, -1.92)\times 10^{-4}$
	$-$	(124.66, 247.22, 0.022)	$(4.6, -2.72, -1.9)\times 10^{-4}$
	$-$	(124.4, 248.57, 0.023)	$(4.4, -2.58, -1.81)\times 10^{-4}$
	$-$	(124.22, 249.57, 0.024)	$(4.25, -2.5, -1.75)\times 10^{-4}$
	$-$	(124.08, 250.32, 0.024)	$(4.15, -2.44, -1.71)\times 10^{-4}$
	$-$	(123.8, 251.91, 0.025)	$(3.97, -2.32, -1.64)\times 10^{-4}$
	$-$	(123.77, 252.06, 0.025)	$(3.96, -2.31, -1.63)\times 10^{-4}$
	$-$	(253.49, 25.76, 8.39)	$(1.15, -1.16, -0.007)\times 10^{-4}$
Field-of-View			
100×100	$+$	(43.5, 51.59, 7.83)	$(-\mathbf{0.024}, 0.017, 5.7\ 10^{-3})$
	$-$	(44.9, 91.1, 0.18)	$(5.5, -2.9, -2.6)\times 10^{-3}$
	$-$	(90.07, 7.59, 14.8)	$(8.8, -8.4, -0.48)\times 10^{-4}$
180×180	$+$	(83.41, 91.8, 7.92)	$(-\mathbf{0.023}, 0.017, 5.5\ 10^{-3})$
	$-$	(77.9, 154.57, 0.025)	$(2.6, -1.64, -0.99)\times 10^{-4}$
	$-$	(161.7, 19.45, 1.16)	$(7.93, -7.72, -2.18)\times 10^{-5}$
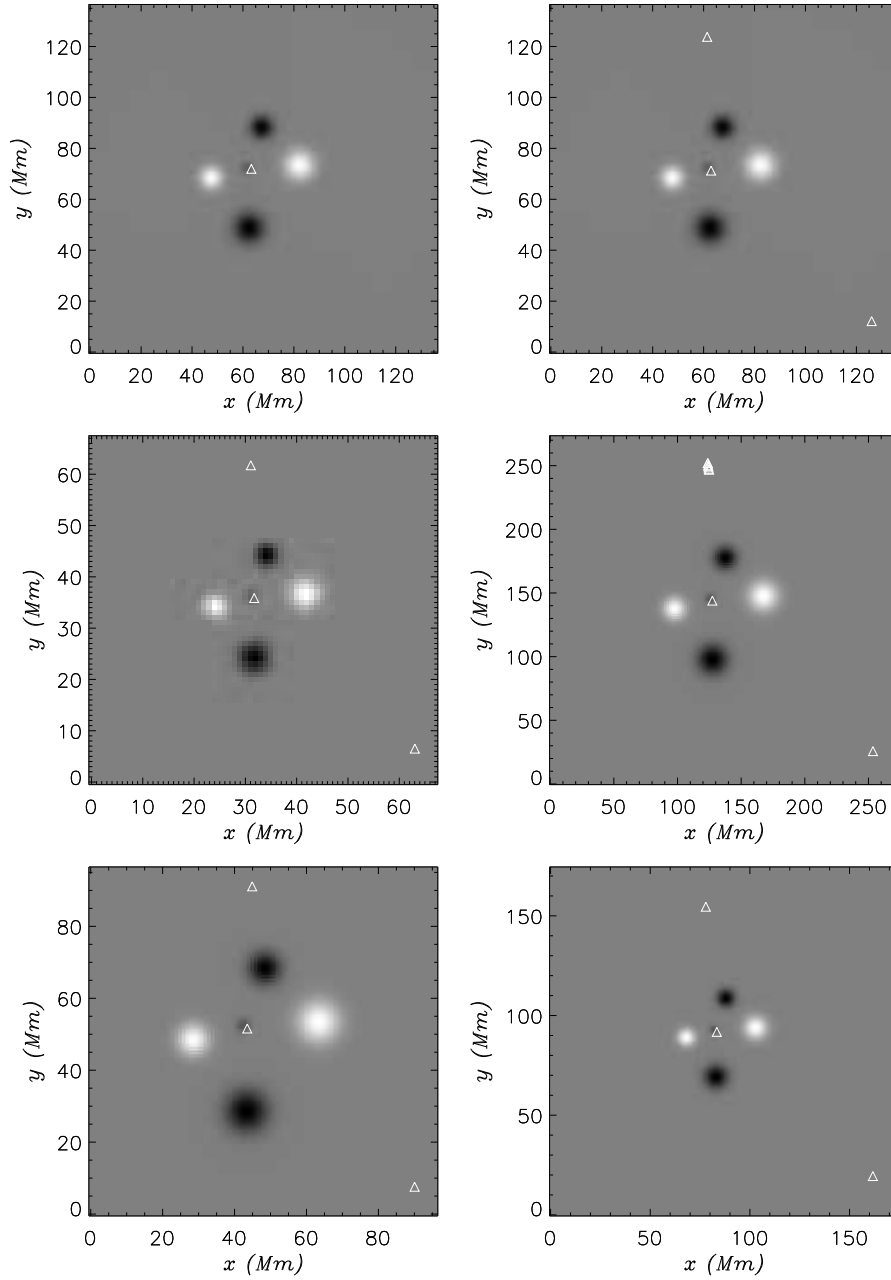
Figure 12. Location of null points (triangles) on the xy-plane for different potential fields. Top row: potential fields with different boundary conditions: (Left) open sides and top boundaries, (Right) periodic. Middle row: potential fields with a different spatial resolution for the same field of view: (Left) decreased by a factor of two, (Right) increased by a factor of two. Bottom row: potential fields for different field-of-view: (Left) reduced by 20 pixels on each edge, (Right) increased by 20 pixels on each edge.